

## Self-similar evolution of a body eroding in a fluid flow

Matthew N. J. Moore, Leif Ristroph, Stephen Childress, Jun Zhang, and Michael J. Shelley

Citation: *Phys. Fluids* **25**, 116602 (2013); doi: 10.1063/1.4829644

View online: <http://dx.doi.org/10.1063/1.4829644>

View Table of Contents: <http://pof.aip.org/resource/1/PHFLE6/v25/i11>

Published by the AIP Publishing LLC.

---

### Additional information on Phys. Fluids

Journal Homepage: <http://pof.aip.org/>

Journal Information: [http://pof.aip.org/about/about\\_the\\_journal](http://pof.aip.org/about/about_the_journal)

Top downloads: [http://pof.aip.org/features/most\\_downloaded](http://pof.aip.org/features/most_downloaded)

Information for Authors: <http://pof.aip.org/authors>

## Self-similar evolution of a body eroding in a fluid flow

Matthew N. J. Moore,<sup>1</sup> Leif Ristroph,<sup>1</sup> Stephen Childress,<sup>1</sup> Jun Zhang,<sup>1,2</sup> and Michael J. Shelley<sup>1</sup>

<sup>1</sup>*Applied Mathematics Laboratory, Courant Institute, New York University, New York, New York 10012, USA*

<sup>2</sup>*Department of Physics, New York University, New York, New York 10003, USA*

(Received 20 June 2013; accepted 20 October 2013; published online 13 November 2013)

Erosion of solid material by flowing fluids plays an important role in shaping landforms, and in this natural context is often dictated by processes of high complexity. Here, we examine the coupled evolution of solid shape and fluid flow within the idealized setting of a cylindrical body held against a fast, unidirectional flow, and eroding under the action of fluid shear stress. Experiments and simulations both show self-similar evolution of the body, with an emerging quasi-triangular geometry that is an attractor of the shape dynamics. Our fluid erosion model, based on Prandtl boundary layer theory, yields a scaling law that accurately predicts the body's vanishing rate. Further, a class of exact solutions provides a partial prediction for the body's terminal form as one with a leading surface of uniform shear stress. Our simulations show this predicted geometry to emerge robustly from a range of different initial conditions, and allow us to explore its local stability. The sharp, faceted features of the terminal geometry defy the intuition of erosion as a globally smoothing process.

© 2013 AIP Publishing LLC. [<http://dx.doi.org/10.1063/1.4829644>]

### I. INTRODUCTION

Erosion by flowing fluids plays an essential role in diverse processes. We most commonly think of erosion in geological contexts, where changing landforms interact with flowing air or water to create a variety of distinct morphologies. Taking the example of a river, a feedback process between the flow and the erodible banks can lead to braided, meandering, or straight channel patterns.<sup>1,2</sup> Likewise, wind erosion helps shape remarkable structures, such as stream-lined ridges known as yardangs,<sup>3,4</sup> or pillar-and-toadstool-shaped rock formations known as hoodoos.<sup>5,6</sup> For yardangs and hoodoos alike, the mutual influence between the shape of the structure and the surrounding flow is thought to be instrumental to development.<sup>4,5</sup> Though less obvious, similar principles are at work in very different settings. For example, plaque structures are subject to erosion and rupture from the flow of blood within arteries,<sup>7,8</sup> and bacterial colonies known as bio-films can be eroded and detached by flowing liquids.<sup>9</sup> Meanwhile, fluid-mechanical erosion is important in the process of chemical-mechanical polishing, which is used in the manufacturing of semiconductor devices.<sup>10</sup>

A feature common to these examples is the coupled evolution of geometry and fluid flow; the fluid flow shapes solid boundaries, which in turn alter the flow. Understanding this reciprocal process in a particular situation requires modeling the physical effects that are present. For example, turbulent entrainment of sediment may be important in the evolution of a river bed, while non-Newtonian flows may be relevant inside the arteries. On the other hand, understanding the interactive nature between shape and flow in an idealized setting may reveal key principles that underly such diverse processes. With this aim, we consider the erosion of canonical geometries held fixed against high-speed, unidirectional fluid flows. This is among the simplest configurations from which to examine the erosion of a solid body, somewhat analogous to the classical Stefan problems of cylindrically or spherically symmetric bodies undergoing melting, dissolution, or other such processes of phase change.<sup>11</sup> Using experiments, theory, and simulations, we find that as the body erodes, it converges

to a terminal form characterized by nearly uniform shear stress, after which it shrinks self-similarly in time.

The present study expands upon previous work by our group involving the erosion of flat beds, cylindrical bodies, and three-dimensional bodies.<sup>12</sup> Here, we focus on two-dimensional erosion of cylindrical bodies, as this case exhibits rich dynamics while at the same time is amenable to mathematical modeling. We present some new experimental measurements and we especially expand our theoretical treatment of the problem, most notably the dynamical simulations that were not discussed previously.

Section II describes experiments performed with centimeter-scale, soft-clay bodies eroding in fast water flows, much like in previous work.<sup>12</sup> Similar to erosion in geological settings, the Reynolds number of our system is large (order 10 000). Further, we observe erosion rates that are many times slower than the flow speed (typically by 5 orders of magnitude), and therefore our experiments preserve the large separation of time-scales present in natural erosion. The experiments show that as a cylindrical body erodes, it evolves into a quasi-triangular shape before ultimately vanishing.

A fluid-mechanical model that takes advantage of the high-Reynolds-number flow allows us to rationalize these observations and extend our understanding of the process. For the cohesive material used in experiments, erosion rate is linearly proportional to the shear stress exerted by the fluid flow, providing the necessary link between flow and body dynamics.<sup>12</sup> As described in Sec. III, our fluid model relies on Prandtl boundary layer theory to decompose the flow field into an inner and outer flow. The outer flow can be treated as inviscid and irrotational (ideal flow), while the inner flow near boundaries is characterized by high shear. We develop an efficient numerical method based on this decomposition to simulate the erosion of a two-dimensional body. In order to model the presence of the wake positioned behind the body, we use free-streamline theory (FST) as originally developed by Helmholtz<sup>13</sup> and Kirchhoff.<sup>14</sup> The outer flow, as determined by the FST method, serves as input into the computation of a boundary layer flow, from which we extract the fluid shear stress and evolve the shape of the body.

The Prandtl decomposition also allows for two key analytical results which we present in Sec. IV. First, simple scaling analysis predicts the area of the body to vanish in finite time as  $(t_f - t)^{4/3}$ , in excellent agreement with experimental measurements. Second, motivated by the wedge-like front seen to develop in experiments, we examine the exactly solvable case of boundary layer flow past an infinite wedge with front angle pointing into the flow. These solutions distinguish a right-angled wedge as having uniform shear stress, which suggests that this shape would shrink self-similarly during erosion. Our previous work made use of these two results,<sup>12</sup> but here we present a more complete description that is largely self-contained.

Section V compares the results of our simulations with experimental measurements of the changing size and shape of the body. Similar to experiments, the simulations show a quasi-triangular geometry to emerge as an attractor of the dynamics. Once formed, this shape undergoes self-similar shrinking and the area vanishes with the predicted 4/3 power law. As the shape develops, the shear stress becomes more evenly distributed along its front surface, and measurements of the simulated body's opening angle show convergence to the predicted right-angle form. Experimental measurements of the opening angle show a similar trend in time, with some differences in the final angle that is reached. Using both simulations and experiments, we examine the influence of initial conditions on shape development, and we find the same terminal form to emerge robustly from different initializations.

## II. THE EXPERIMENTS

We first discuss laboratory experiments in which clay bodies are held fixed against a high-speed water flow.<sup>12</sup> Here, we focus on the case of nearly two-dimensional erosion in which a cylinder of clay is placed within the laminar, unidirectional flow generated by a water tunnel. Our experimental design allows for both flow visualization as well as measurements of how the clay body shrinks and changes shape as it erodes.

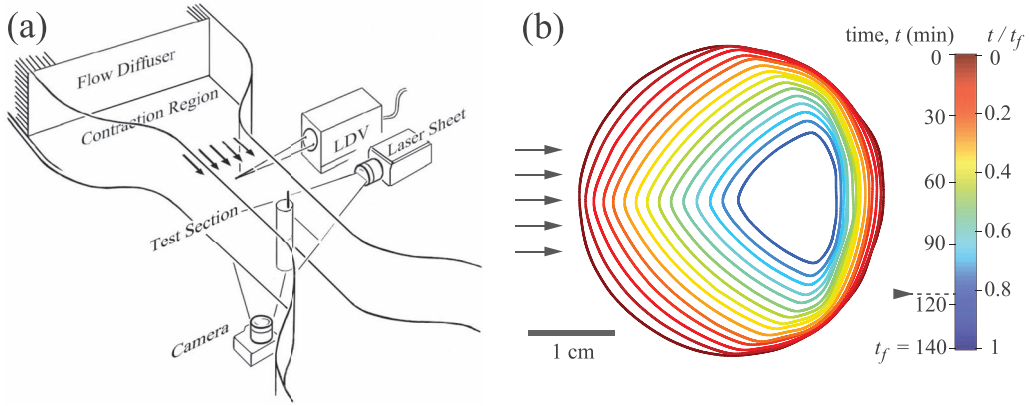


FIG. 1. Experimental study of the erosion of a clay cylinder in flowing water. (a) A water tunnel provides a unidirectional flow, and the cross-section of the cylinder is photographed every minute. Flow speed is monitored using a laser Doppler velocimeter (LDV). To visualize the flow, particles are added to the water and illuminated with a laser sheet. (b) Shrinking and shape change during erosion (adapted from Ristropf *et al.*<sup>12</sup>). Interfaces extracted from photographs show the cross-section of the body at intervals of 8 min. Interfacial data are extracted through 115 min (indicated by the arrow on the color bar), and the projected time at which the body would vanish entirely is  $t_f = 140 \pm 2$  min.

### A. Experimental apparatus and methods

The schematic of Fig. 1(a) shows the key features of our experimental apparatus, which was also used in our earlier study.<sup>12</sup> The flow is furnished by a recirculating water tunnel that pumps water across a transparent test section measuring  $15 \times 15 \times 43$  cm (width  $\times$  height  $\times$  length). An upstream diffuser and contraction region ensures a low-turbulence flow of nearly uniform velocity in space. Prior to running erosion experiments, we use a laser Doppler velocimeter (LDV; TSI Inc.) to characterize the flow speed fluctuations. For the speed selected in this study, typical fluctuations in time were measured to be 1.3%. Similarly, variations in speed along both the vertical and horizontal directions are less than 1.8% for locations at least 1 cm from the walls.

To form the erodible body, we combine distilled water and bentonite nanoclay powder (Sigma-Aldrich) in a 3:2 mixture by weight. This recipe yields a material that is soft enough to erode over an experimentally convenient time-scale, yet stiff enough to support itself against the flow. We sculpt the clay into a circular cylinder using a custom-made lathe and slightly taper the bottom portion of the body. The taper ensures an unobstructed view of the body's mid-height cross-section by a camera that is situated below the test section (see Fig. 1(a)). During the experiments, the clay cylinder is supported vertically in the water tunnel against a flow speed of  $U_0 = 61$  cm/s, which is monitored by LDV. Erosion of the clay causes the water to become turbid, and in order to preserve image clarity, we continuously drain the turbid water while adding fresh water. By adjusting the temperature of this incoming water, we are able to maintain the tunnel temperature at  $28 \pm 1$  °C throughout the experiment.

Our experiments preserve two important characteristics of erosion in natural scenarios. First, the Reynolds number is large. We use a cylinder of initial diameter  $2a_0 = 3.6$  cm, yielding  $Re = 2U_0a_0/\nu = 3 \times 10^4$ , where  $\nu = 8 \times 10^{-3}$  cm<sup>2</sup>/s is the kinematic viscosity of water. During these experiments, the body shrinks in width to roughly 1/3 its initial value, so Re remains large. Second, erosion occurs very slowly compared to the flow. Solid boundaries recede at typical rates of  $V_n \sim 1$  cm/hr, which when compared to the flow speed  $U_0$ , gives a ratio of  $V_n/U_0 \sim 5 \times 10^{-6}$ .

### B. Interfacial dynamics and flow visualization

In our first set of experiments, we examine how the shape of the body changes during erosion. We photograph the cross-section of the body at mid-height every minute and use a custom image-analysis routine to extract cross-sectional interfaces. Although its shape changes, the body remains nearly cylindrical throughout the experiment. In Fig. 1(b), we show the interfaces at intervals of

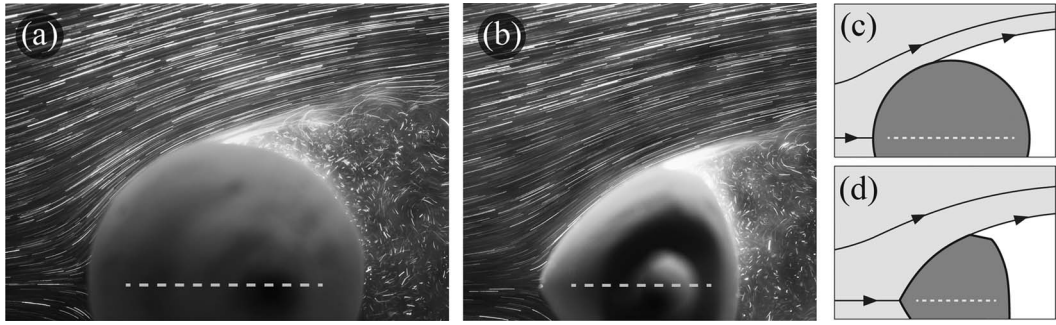


FIG. 2. Visualizing the flow around a cylindrical body at different times in the erosion process. Streaklines are captured by 10 ms exposure time photographs of tracer particles illuminated by a laser sheet, and the initial diameter of the body is 3.6 cm. (a) Early in the process,  $t = 5$  min, the incoming flow stagnates at the nose and conforms to the body until separating just upstream of the widest portion. The wake behind the body consists of a relatively slow and unsteady flow. (b) At  $t = 55$  min, the body has formed a quasi-triangular shape, yet the flow structure is qualitatively similar. The flow stagnates at the nose and separates near the body's widest portion, in this case near the back corners of the triangular shape. (c) and (d) Flow schematics.

8 min and color coded in time (color). Data are shown through 115 min at which time the support pole obstructs the view of the body's cross-section. As seen in the figure, erosion leads to an overall shrinkage of the body in time, and differential removal rates along the surface lead to changes in shape. In particular, the initially round boundary is carved into a quasi-triangular shape with one corner located at the nose and a corner on each side of the body. The front of the body is thus wedge-like and pointing into the flow, and erosion occurs predominately along these surfaces. The backside experiences relatively weak erosion rate and does not change shape as significantly. Nonetheless, interesting facets are seen to develop immediately behind the back corners, causing the body to appear somewhat pentagonal.

To relate these interfacial dynamics to the surrounding fluid, we visualize the flow field with tracer particles. The particles (glass microspheres of typical size  $40 \mu\text{m}$ ) are illuminated by a laser sheet at the mid-height of the tunnel and photographed with an exposure time of 1/100 s. The images in Figs. 2(a) and 2(b) reveal the flow streaklines early in the experiment (5 min) and later (55 min) when the body has eroded significantly. The corresponding schematics of Figs. 2(c) and 2(d) highlight some important flow features. Early in the process, the incoming flow stagnates at the front, conforms to the body along the cheeks, and separates just upstream of the widest portion of the cylinder. The wake sits downstream of the body and consists of a relatively slow and time-dependent flow. These features are similar to those observed for rigid cylinders at comparable Reynolds numbers, indicating that the material removal process does not strongly influence the instantaneous flow structure. Similar flow features can be seen around the quasi-triangular body that is formed later in the experiments. Again, the flow is characterized by a stagnation point at the nose, two separation points on either side of the body, and a relatively slow wake. In this case, flow separation occurs near the side corners on the body, and the facets sit immediately behind these corners.

In Sec. V, we will present further analysis of the interfaces in Fig. 1(b). In particular, we will quantify the body's cross-sectional area in time and compute the instantaneous material-removal rate as a function of the arc length. These results will be compared with results from a fluid mechanical model of erosion, which we present next.

### III. THE MODEL

Here, we outline the main concepts underlying our fluid mechanical model of erosion. The first main ingredient is a constitutive law relating solid body erosion to the surrounding fluid flow. For the clay material used here, previous experiments<sup>12</sup> have shown the local rate of material removal to be linearly proportional to the absolute fluid shear stress,  $|\tau|$ . Thus, at an instant in time, the solid

boundary recedes with a local normal velocity given by

$$V_n = -C |\tau|, \quad (1)$$

where  $C$  is a material-dependent constant (i.e., the erodibility). This law is similar to others that can be found in the literature,<sup>15,16</sup> which sometimes incorporate additional parametric dependencies, such as a power for the shear stress and/or a threshold shear stress below which material does not erode.

For high-Reynolds-number flows, shear stress is associated with a thin boundary layer surrounding the body, and we therefore use Prandtl boundary layer theory as the foundation of our model. Further, since we observe the body to remain cylindrical throughout our experiments, we treat the fluid flow as two dimensional. In the following, we outline the main ideas from Prandtl theory needed in our model, and then we describe a simulation method based on those ideas. The Prandtl framework allows for certain analytical results which we present in Sec. IV, before presenting the main results of the simulations in Sec. V.

### A. The Prandtl decomposition

The fluid flow exterior to the cylindrical body is governed by the 2D incompressible Navier-Stokes equations,

$$\frac{\partial \mathbf{u}}{\partial t} + (\mathbf{u} \cdot \nabla) \mathbf{u} = -\frac{1}{\rho} \nabla p + \nu \nabla^2 \mathbf{u}, \quad (2)$$

$$\nabla \cdot \mathbf{u} = 0, \quad (3)$$

$$\mathbf{u} = 0 \quad \text{on } \partial B \quad (4)$$

$$\mathbf{u} \rightarrow (U_0, 0) \quad \text{as } |\mathbf{x}| \rightarrow \infty. \quad (5)$$

We model erosion by allowing solid material on the boundary,  $\partial B$ , to become fluidized. New fluid parcels are introduced into the fluid domain with zero momentum, giving the vanishing boundary condition (4). Far away from the body, the velocity field matches the free-stream value  $U_0$ , as in Eq. (5). Owing to the large separation of time-scales between erosion rate and flow rate, we treat the fluid flow as quasi-steady by setting  $\partial_t \mathbf{u} = 0$  hereafter.

Prandtl boundary layer theory provides a well-established framework to analyze high-Re flows by partitioning the fluid domain into an outer and inner region, as diagramed in Fig. 3(a). In the outer region, sufficiently far from boundaries and excluding the wake, the flow can be treated as inviscid, i.e.,  $\nu = 0$  in Eq. (2). If the outer velocity field,  $\mathbf{u}_o$ , is initially irrotational,  $\nabla \times \mathbf{u}_o = 0$ , then it remains irrotational at later times and can be described by a velocity potential,  $\mathbf{u}_o = U_0 \nabla \phi$ , where

$$\nabla^2 \phi = 0, \quad (6)$$

$$\nabla \phi \cdot \hat{\mathbf{n}} = 0 \quad \text{on } \partial B \quad (7)$$

$$\nabla \phi \rightarrow (1, 0) \quad \text{as } |\mathbf{x}| \rightarrow \infty. \quad (8)$$

The outer flow has vanishing normal velocity on the boundary, as indicated by the Neumann condition (7). However, since the outer flow is inviscid, it may have a tangential, slip velocity, given by

$$U(s) = \hat{\mathbf{s}} \cdot \mathbf{u}_o |_{\partial B}. \quad (9)$$

Here,  $s$  is arc length along the boundary with unit direction  $\hat{\mathbf{s}}$ . The outer, tangential velocity,  $U$ , along with its derivative,  $U' = dU/ds$ , will facilitate the determination of the inner flow.

The inner region consists of a thin layer surrounding the solid boundaries, as shown in Figs. 3(a) and 3(b). Here, the effects of viscosity come to bear, and scaling analysis of the

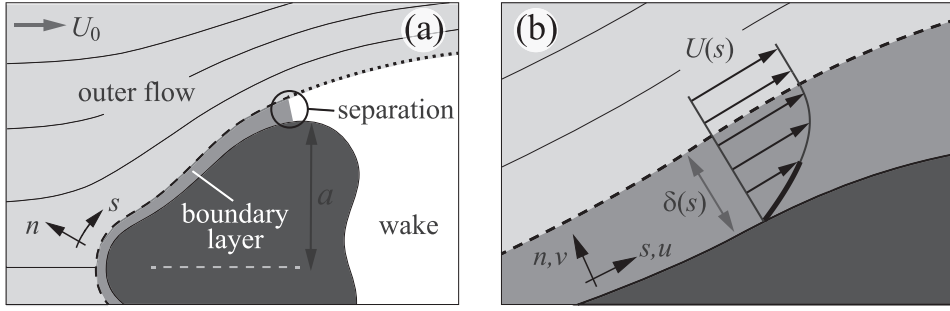


FIG. 3. High-Re flow past a bluff body in two dimensions. (a) The fluid flow is comprised of an outer and boundary layer flow, with the dashed curve indicating the thickness of the boundary layer. At the separation point, the boundary layer detaches and a wake is formed. The dotted curve represents the separating streamline. (b) Zoom into the boundary layer. The velocity profile inside the boundary layer approaches the outer tangential velocity  $U(s)$  at a characteristic distance  $\delta(s)$ . Fluid shear stress is proportional to the slope of the velocity profile at the surface (darkened).

Navier-Stokes Eqs. (2)–(4) leads to the Prandtl boundary layer equations<sup>17,18</sup>

$$u \frac{\partial u}{\partial s} + v \frac{\partial u}{\partial n} - v \frac{\partial^2 u}{\partial n^2} = U U', \quad (10)$$

$$\frac{\partial u}{\partial s} + \frac{\partial v}{\partial n} = 0. \quad (11)$$

As diagrammed in Fig. 3(b),  $(s, n)$  are the tangential and normal surface coordinates with corresponding velocity components  $(u, v)$  of the inner flow. The Prandtl equations hold within a boundary layer of thickness,  $\delta(s)$ , which has characteristic scale,<sup>17,18</sup>

$$\delta^* = \sqrt{\frac{va}{U_0}}. \quad (12)$$

Here,  $a = a(t)$  is a characteristic length-scale of the body which we take to be half the width transverse to the flow; e.g., for the case of a circle,  $a$  is simply the radius. Boundary conditions for Eqs. (10) and (11) include

$$u(s, 0) = v(s, 0) = 0, \quad (13)$$

$$u(s, n) \rightarrow U \quad \text{as } n/\delta^* \rightarrow \infty, \quad (14)$$

$$\frac{\partial^2 u}{\partial n^2}(s, 0) = -\frac{1}{v} U U'. \quad (15)$$

Equation (13) is simply a restatement of the no-slip boundary condition (4), while Eq. (14) is a matching condition for the inner and outer velocity fields. Equation (15) results from evaluating Eq. (10) at  $n = 0$  and enforcing condition (4). With the inner flow determined by Eqs. (10)–(15), the shear stress on the solid boundary is given by

$$\tau(s) = \nu \rho \frac{\partial u}{\partial n}(s, 0). \quad (16)$$

As expressed in this formula, shear stress is proportional to the slope of the velocity profile at the surface, which we highlight in Fig. 3(b). Note that it is  $|\tau|$  that enters the constitutive law of Eq. (1). Thus, based simply on this law, one would expect corners to form at points where  $\tau$  vanishes, including at the nose and at the separation points.

## B. Outline of simulation method

The Prandtl decomposition offers a significant simplification of the original Navier-Stokes system, which can be exploited to efficiently compute the fluid flow and simulate the erosion

process. Due to the quasi-steady assumption, we need only compute the steady flow field around a given shape, and thus our method consists of three steps:

1. Given the body shape at some time, determine the surrounding steady fluid flow.
2. From the fluid flow, determine the shear stress,  $\tau$ , along the solid boundary.
3. Evolve the boundary according to the erosion law, Eq. (1), and return to step 1.

In this section, we outline the main ideas of the method, while we present a more detailed explanation of the numerical methods in the Appendix.

Our Prandtl-based method must confront the subtlety of how to model the wake, where shed vorticity from the boundary layer causes the irrotational assumption of the outer flow to be violated. The FST<sup>19–21</sup> offers a means of solution by postulating that the boundary layer separates to form “free” streamlines which enclose the wake (see Fig. 3(a)). Ideal flow holds outside of the wake, while inside assumptions must be made regarding the distributions of vorticity and pressure.<sup>22–24</sup> Here, we use the relatively simple Helmholtz/Kirchhoff (HK) model,<sup>13,14</sup> which assumes a stagnant wake of infinite extent, inside of which pressure is equal to its far field value,  $p_0$ . This minimal set of assumptions is appealing from a modeling perspective, and, moreover, the HK model is considered a plausible candidate for separated-flow structure in the limit of infinite Reynolds number.<sup>19</sup>

In the outer region, the velocity field is steady potential flow, and thus the steady Bernoulli equation applies throughout

$$p + \frac{1}{2}\rho |\mathbf{u}_o|^2 = p_0 + \frac{1}{2}\rho U_0^2. \quad (17)$$

By continuity, the pressure on the free streamlines is equal to the value in the wake,  $p_0$ , and therefore Bernoulli’s equation implies that  $|\mathbf{u}_o| = U_0$  on the free streamlines. In terms of the potential, this condition becomes

$$|\nabla\phi| = 1 \quad \text{on the free streamlines.} \quad (18)$$

As detailed in the Appendix, our FST method uses conformal mapping techniques to simultaneously determine the positions of the free streamlines and the velocity potential through the numerical solution of Eqs. (6)–(8), and (18). To uniquely determine the free streamlines, it is necessary to specify the points on the body at which the flow initially separates. For this, we use the Brillouin–Villat (BV) condition,<sup>19,25,26</sup> a regularity condition requiring the curvature of the free streamlines to match that of the body at the separation points. The numerically determined outer flow then feeds into the Prandtl PDEs, Eqs. (10)–(15), which we solve approximately with the von Kármán–Pohlhausen (VKP) method.<sup>18,27,28</sup> The VKP method relies on similarity transform and vertical integration of the Prandtl PDEs to obtain an ordinary differential equation (ODE) for boundary layer thickness. We solve this ODE numerically and extract the shear stress, which we then use to evolve the boundary through Eq. (1). Since Eq. (1) depends on  $|\tau|$ , corners are expected to form near the stagnation and the separation points. Meanwhile, our FST method requires smooth bodies, and so to regularize boundary evolution we introduce a term involving the local body curvature into Eq. (1) – a technique that is often used in problems of front propagation.<sup>29,30</sup> As a result, our simulation allows the development of corner-like features that are smooth on a fine scale.

In Sec. V, we will describe the results of the simulation in terms of dimensionless quantities, with the outer velocity scaled on  $U_0$  and length scaled on  $a_0$  (the initial value of  $a(t)$ ). In order to non-dimensionalize the quantities describing the inner flow, we use a *fixed* characteristic boundary layer thickness given by

$$\delta_0^* = \sqrt{\frac{\nu a_0}{U_0}} = \sqrt{\frac{2}{\text{Re}}} a_0. \quad (19)$$

Here, we have simply replaced  $a(t)$  by  $a_0$  in Eq. (12). We use Eq. (16), to estimate a fixed characteristic shear stress as  $\tau_0^* = \nu\rho U_0/\delta_0^*$ , giving

$$\tau_0^* = \rho \sqrt{\frac{\nu U_0^3}{a_0}} = \sqrt{\frac{2}{\text{Re}}} \rho U_0^2. \quad (20)$$

For body evolution, we use a characteristic interface velocity,  $V_n^* = C\tau_0^*$ , with an associated erosion time-scale,  $t^* = 2a_0/V_n^*$ . In terms of physical parameters,  $t^*$  is given by

$$t^* = \frac{2}{C\rho} \sqrt{\frac{a_0^3}{\nu U_0^3}}. \quad (21)$$

An advantage of scaling time on  $t^*$  is that there is no need to specify values of  $\text{Re}$  and  $C$  in our simulations. Rather, the simulations apply to the asymptotic regime of  $\text{Re} \gg 1$  and  $V_n^* \ll U_0$ , which reduces the parameter space significantly.

#### IV. ANALYTICAL RESULTS

Before presenting the results of the simulations, we present in this section two key analytical predictions related to the size and shape of the eroding body. The first is a scaling law for the body's vanishing rate, and the second is a prediction for its terminal form. These analytical results will provide a useful base of comparison for both the experiments and simulations.

##### A. Scaling analysis for vanishing rate

The Prandtl framework allows for relatively simple scaling analysis to predict the area of the eroding body in time.<sup>12</sup> The time-dependent shear stress can be estimated as

$$\tau^* = \rho \sqrt{\frac{\nu U_0^3}{a(t)}}. \quad (22)$$

Thus, as the body erodes and  $a(t) \rightarrow 0$ , the overall shear stress grows larger. The rate at which the body area,  $A(t)$ , decreases in time can be estimated by the shear stress times the exposed perimeter, giving  $dA/dt \sim -\tau^* a$ . Inserting Eq. (22), and only retaining scaling with respect to  $a$ , gives  $dA/dt \sim -\sqrt{a} \sim -A^{1/4}$ , which has solution,

$$A(t) \sim A_0 \left(1 - \frac{t}{t_f}\right)^{4/3}. \quad (23)$$

Thus, Prandtl theory predicts area to follow a 4/3-power law in time, decreasing from an initial value  $A_0$  and vanishing at time  $t_f$ . This prediction can be compared to experiments by measuring the cross-sectional area of the interfaces from Fig. 1(b). In Fig. 4(a), we show the experimental area measurements plotted against time, along with the predicted scaling law. The two shows excellent agreement, supporting the assumptions of our model as well as the shear-stress dependent erosion law. Although the experiments cannot be run until  $t_f$  (due to the size of the supporting rod), Eq. (23) allows us to extrapolate the measurements to estimate the vanishing time as  $t_f = 140 \pm 2$  min. Plotting the normalized area measurements against  $1 - t/t_f$  on a log-log scale, as in Fig. 4(b), shows further confirmation of the predicted 4/3 power. We note that  $t_f$  is simply a multiple of the basic time-scale  $t^*$  from Eq. (21).

##### B. Exact solutions for shear stress on wedges

The emergence of a wedge-like front in the experiment (see Fig. 1(b)) motivates us to theoretically examine flow past a wedge. Within the Prandtl framework, the so-called Falkner-Skan similarity solutions<sup>31</sup> can be used to determine the shear stress along an infinite wedge that points

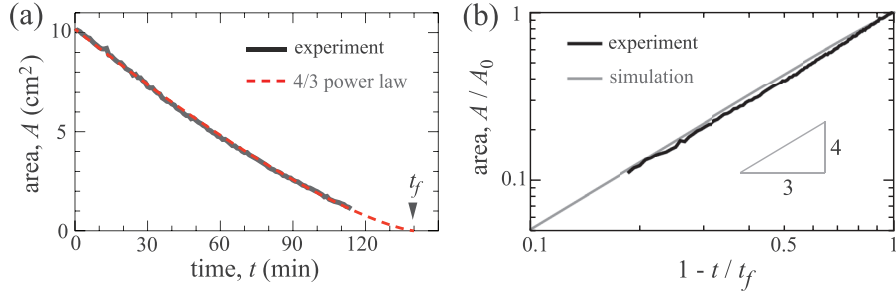


FIG. 4. Body area versus time. (a) Area measurements of the experimental interfaces from Fig. 1(b) (black) show excellent agreement with the scaling law from Eq. (23) (dashed, red) (adapted from Ristroph *et al.*<sup>12</sup>). This formula allows us to estimate the vanishing time,  $t_f$ , from the experiments. (b) Log-log plot of the area measurements from the experiment (black) and simulation (gray). Both match the 4/3-power prediction.

symmetrically into the flow. While our previous work made reference to this class of solutions,<sup>12</sup> here we provide a more complete description that is largely self-contained.

As can be determined by elementary conformal mapping,<sup>18</sup> the outer, tangential velocity along a wedge with opening angle  $2\alpha$  is given by  $U(s) = c_0 s^m$ , where  $m = \alpha/(\pi - \alpha)$ ,  $c_0$  is a constant, and  $s$  is arc length from the nose. For the inner flow, let a stream-function  $\psi$  be defined by  $u = \partial_n \psi$  and  $v = -\partial_s \psi$ . In terms of  $\psi$ , the Prandtl equation (10) becomes

$$\frac{\partial \psi}{\partial n} \frac{\partial^2 \psi}{\partial n \partial s} - \frac{\partial \psi}{\partial s} \frac{\partial^2 \psi}{\partial n^2} - v \frac{\partial^3 \psi}{\partial n^3} = mc_0^2 s^{2m-1}. \quad (24)$$

Introducing the similarity variable,  $\eta = n/\delta_s$ , where  $\delta_s = \sqrt{vs/U}$ , and expressing the stream-function as  $\psi = \sqrt{vsU} f(\eta)$  reduces Eq. (24) to an ODE for  $f(\eta)$ ,

$$f''' + \frac{1}{2}(m+1)ff'' - mf'^2 + m = 0. \quad (25)$$

From Eq. (16), the shear stress is given by

$$\tau(s) = c_1 s^{(3m-1)/2}. \quad (26)$$

The constant is given by  $c_1 = \rho \sqrt{vc_0^3} f''(0)$ , where  $f''(0)$  may be determined by the numerical solution of Eq. (25), subject to boundary conditions.<sup>18</sup>

This constant, however, is not needed to understand how the shear stress depends on the wedge's opening angle,  $2\alpha$ . For an acute angle,  $\alpha < \pi/4$ , the exponent in Eq. (26) is negative, implying highest shear stress near the nose,  $s = 0$ . In Fig. 5(a), we illustrate the velocity field around a narrow wedge,

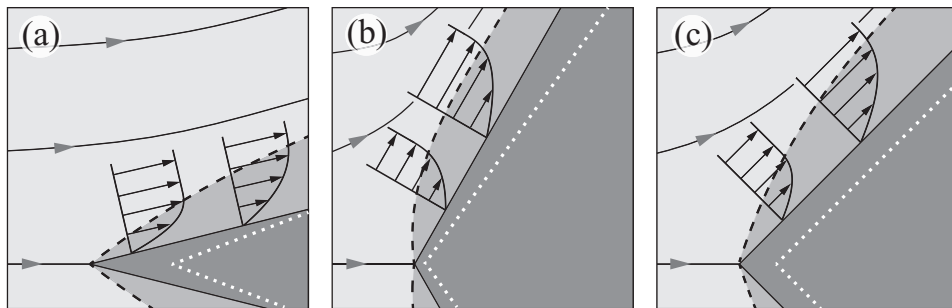


FIG. 5. Falkner-Skan similarity solutions for flow past wedges. (a) Illustration of the outer and boundary-layer flow past a wedge with acute opening angle. The shear stress is highest near the nose as indicated by the surface slopes of the velocity profiles. This causes the wedge to broaden as it erodes, which we indicate by the white dotted wedge. (b) For an obtuse opening angle, the shear stress increases downstream, and the wedge tends to become more narrow at later times. (c) A right-angled wedge produces uniform shear stress, which allows the shape to be maintained during erosion.

where the profile surface slopes indicate that shear stress decreases downstream. Since the nose of such a wedge erodes faster than the downstream portion, the body will tend to broaden during the course of evolution, which we indicate by the white dotted wedge in the figure. On the other hand, an obtuse angle,  $\alpha > \pi/4$ , gives a positive exponent in Eq. (26), resulting in a shear stress that increases downstream. Figure 5(b) illustrates the velocity field for this case, and indicates that such a wedge will tend to become narrower at later times. Interestingly, an opening angle of  $90^\circ$  causes the exponent in Eq. (26) to vanish, which implies uniform shear stress along the surface of the wedge. With uniform shear stress, the boundary would recede at the same rate everywhere, allowing the shape to be maintained (see Fig. 5(c)). In this way, a right-angled wedge front is a candidate for the terminal form of an eroding body. Moreover, the observation that an acute wedge will tend to become broader and an obtuse wedge will narrow suggests stability of the right-angled front.

## V. SIMULATION RESULTS

Dynamical simulation provides a controlled setting in which to compare our model to the experiments and to test the above analytical predictions. In this section, we present the main results of the simulation, with the detailed explanation of the numerical methods provided in the Appendix.

### A. Erosion of an initially circular body and comparison to experiments

First, for comparison with the experiments, we simulate the erosion of an initially circular body. In Fig. 6(a), we show the evolution of the eroding body at equally spaced time intervals. As the body shrinks, it morphs into a triangular shape pointing into the flow, much like that seen in the experiments. In our simulation, no erosion occurs on the backside due to the assumption that the wake is stagnant, and this is in reasonable accordance with the relatively slow erosion observed on the body's back in experiments (see Fig. 1(b)). Unlike the experiment, the simulation permits us to observe body evolution up until the time of vanishing. It is clear in Fig. 6(a) that at later times the distance between successive interfaces grows larger. This observation is consistent with a shear stress that increases with decreasing body size as in Eq. (22). To test this scaling quantitatively, we plot in Fig. 4(b) the area of the interfaces against rescaled time,  $1 - t/t_f$ , which demonstrates excellent agreement between the simulation and the predicted 4/3-power law of Eq. (23), as well as with the experimental measurements of area.

To more clearly illustrate how the body changes shape, we show in Fig. 6(b) the interfaces shifted to have the same leading point and rescaled to have equal area. As seen in the figure, the front morphs rapidly to its wedge-like form, while evolution proceeds more slowly further back on

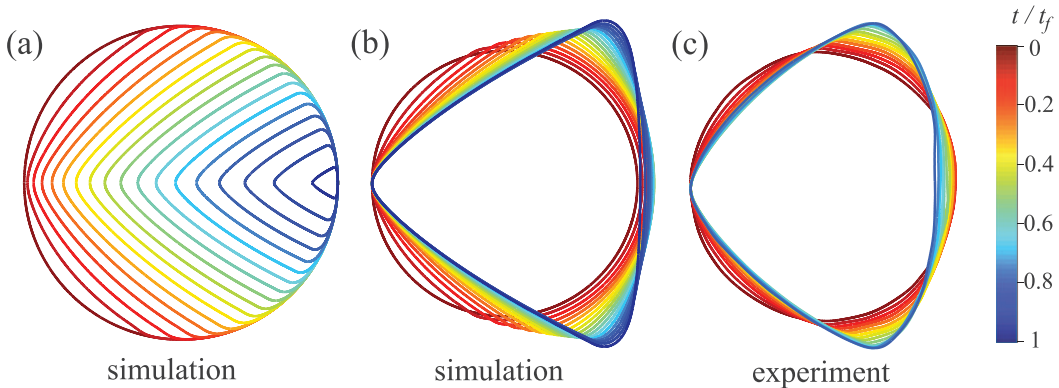


FIG. 6. Erosion of an initially circular body. (a) Interfaces from the simulation at evenly spaced time intervals of  $0.06 t_f$ , with time indicated by the scale bar at right (color). As it shrinks, the body forms a quasi-triangular shape with a wedge-like front that points into the flow. (b) Shifting the interfaces to have the same leading point and rescaling to have equal area more clearly reveals the shape change. (c) The same rescaling procedure applied to the experimental interfaces shows similar evolution and terminal shape.

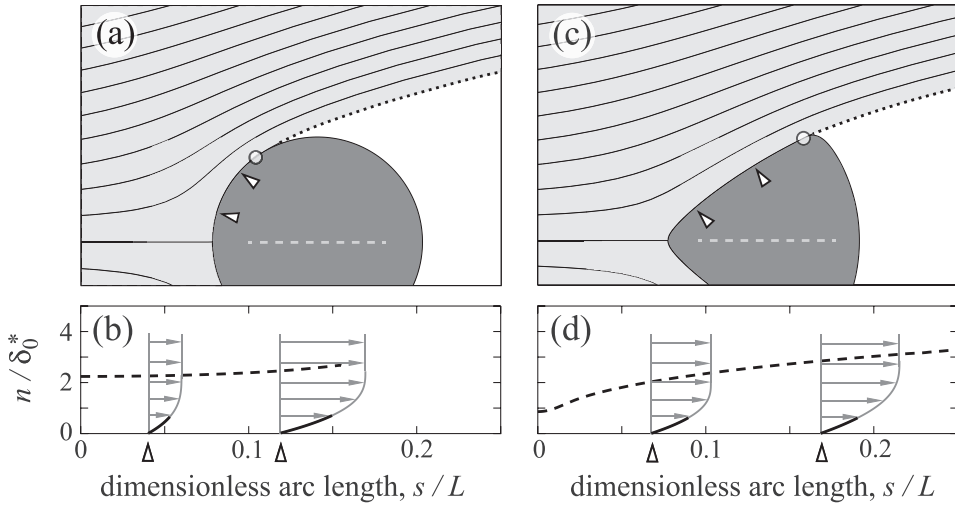


FIG. 7. Computed flows at different stages of erosion. (a) The streamlines of the outer flow as determined by the FST method for the initial, circular geometry. The flow accelerates as it deflects around the body, as can be seen by the compression of streamlines. The small circle on the body indicates the separation point and the dotted curve shows the free streamline. The blank region behind the body represents the stagnant wake. (b) Boundary layer flow for the above body. The dashed curve shows the computed boundary layer thickness against normalized arc length,  $s/L$ , along the front of the body. This dashed curve ends at the point of flow separation. We also show the computed velocity profile at two points on the body (indicated by arrows in (a)), demonstrating that the shear stress varies along the surface of this body. (c) By time  $t/t_f = 0.64$ , the body has developed a wedge-like front and the separation point has migrated backwards. (d) For this body, the velocity profiles indicate little variation in the shear stress.

the body. For comparison, Fig. 6(c) shows the same shifting-and-rescaling procedure applied to the experimental interfaces of Fig. 1(b). Even though the experiment cannot be run all the way to  $t_f$ , the comparison is qualitatively good. Both experiment and simulation show a terminal form that resembles a triangle, with the experimental body having a somewhat broader front than does the simulated body. In Subsection V B, we will further quantify this comparison through measurements of the front opening angles.

The simulation enables us to examine the fluid flow that is computed around the evolving body and compare it to the experimental flow visualizations. In Fig. 7(a), we show the outer flow as computed by our FST method for the initial, circular geometry. Streamlines become compressed as they deflect around the body, indicating an accelerating outer flow. The small circle on the body shows the point of flow separation and the dotted curve indicates the free streamline that divides the region of ideal flow from the stagnant wake. The overall structure of this computed flow field compares quite well with the experimental flow visualization of Fig. 2(a). While the boundary layer flow is too small to be resolved in the experimental photograph, the simulation allows for a view into the boundary layer. Figure 7(b) shows the computed boundary layer thickness along the surface of the body, with arc length starting from the leading point and normalized by the total perimeter length  $L$ . Evidently, the circular geometry produces a boundary layer of relatively constant thickness.

Figure 7(c) shows the body and its surrounding flow at a later stage of development. By this time, the wedge-like front has formed and the separation point has migrated backwards on the body. These features, as well as the qualitative structure of the surrounding flow field, agree quite well with experimental visualization of Fig. 2(b). In the simulation, the downstream migration of the separation point results from applying the BV condition to an evolving body, which illustrates the key role this condition plays in our model. For this wedge-like geometry, Fig. 7(d) shows that the boundary layer grows in the downstream direction.

Why does the wedge-like front emerge from the erosion dynamics? Monitoring the distribution of the interface velocity,  $V_n$ , gives some insight into this question. In Fig. 8(a), we plot  $V_n$  along the simulated body early on when it is circular (red), and later once the triangular form has developed (blue). As time proceeds,  $V_n$  becomes nearly uniform along the front of the body, while it always

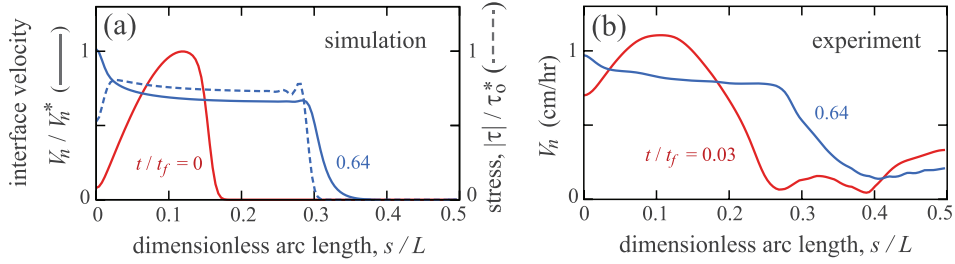


FIG. 8. Tendency towards uniform erosion rate. (a) The simulation interface velocity as it varies along the body's arc length at time  $t/t_f = 0$  (red) and 0.64 (blue). Also shown is the shear stress at the later time (dashed curve, blue, axis at right). Both interface velocity and shear stress become more uniform at the later time. (b) Measurements of the interface velocity against arc length from the experiments at time  $t = 4$  min (red) and 90 min (blue), corresponding to  $t/t_f = 0.03$  and 0.64. The experimental measurement also shows the local erosion rate to become more uniform at later time (adapted from Ristropf *et al.*<sup>12</sup>).

vanes along the backside. This allows the front to essentially recede as a whole, and, in this way, the shape of the body is preserved. For comparison, we also calculate the interface velocity in the experiments by measuring the distance between successive interfaces. Figure 8(b) shows these measurements of  $V_n$  early on, when the body is circular (red), and later, when it is near the terminal form (blue). At the later time, the interface velocity is nearly uniform along the front, much like in the simulation, and the comparison between the two is reasonably good.

The simulation enables us to also monitor the shear stress as it varies along the evolving body. Figure 8(a) shows that the shear-stress distribution, much like the interface velocity, becomes more uniform as the quasi-triangular geometry develops (dashed curve, right axis). In our simulation, interface velocity and shear stress only differ by the curvature term that was introduced for regularity (see Eq. (A28)). Interestingly, this term accounts for an increase in  $V_n$  near the nose that is also observed in the experiments. This observation suggests that the curvature-dependent term may carry some physical significance, and we discuss this possibility further in Sec. VI. We note that in Fig. 8(a), the distribution  $|\tau|$  has been smoothed by a narrow Gaussian filter in  $s$  (see Subsection A 2 of the Appendix for details), which is why it does not vanish at the front stagnation point.

Returning to the flow fields of Fig. 7, the computed boundary-layer flow gives insight into how the quasi-triangular geometry produces uniform shear stress. For this geometry, Fig. 7(d) shows that the boundary layer is smallest at the nose and increases in the downstream direction. Since the outer flow accelerates downstream, the increasing boundary-layer size allows the shear stress to remain relatively constant. As illustration of this idea, we plot in Fig. 7(d) the velocity profile computed by our VKP method at two points along the body (indicated by arrows). Although the profiles themselves are not identical, they have similar slopes at the surface, which indicates similar values of shear stress. In contrast, the circular geometry produces a relatively constant boundary layer thickness (see Fig. 7(b)), which, combined with the accelerating outer flow, leads to variable shear stress. Indeed, the two velocity profiles shown in Fig. 7(b) do not have similar surface slopes, indicating different shear-stress values.

## B. Opening angle of the wedge

As demonstrated above, erosion shapes bodies to more evenly distribute the shear stress. Meanwhile, the exact solutions from Sec. IV B predict that an infinite, right-angled wedge produces uniform shear stress, and it is interesting to consider whether this prediction has some bearing for finite bodies. We therefore seek to estimate the opening angle of the wedge-like shapes that develop in our simulations. For a given body, we fit the middle third of the upper and lower faces with circle arcs, and measure their intersection angle  $\Psi$ . This shape, known as an *ogive*, provides a good characterization of the eroding body's front, as Fig. 9(a) demonstrates. In Fig. 9(b), we plot  $\Psi$  as it varies in time during the simulation (gray). Initially, the opening angle decreases rapidly, as the front of the body morphs from the original flat state,  $\Psi = 180^\circ$ , to a wedge-like form. In long time, the

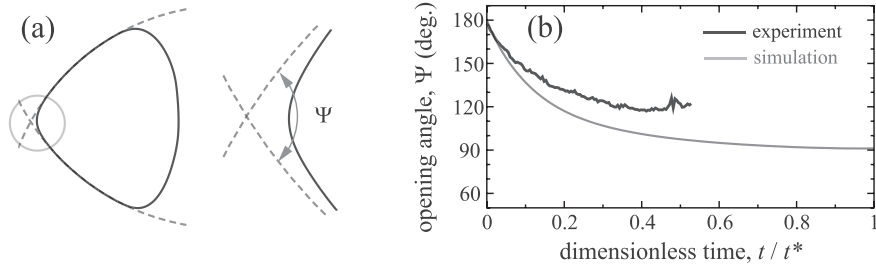


FIG. 9. Opening angle measurements. (a) The opening angle is measured by fitting the upper and lower faces of the front with circle arcs, and finding the angle of intersection between the arcs. (b) The angle measurement,  $\Psi$ , versus dimensionless time,  $t/t^*$ , for the simulation (gray) and experiment (black).

angle approaches an asymptote of  $\Psi = 91^\circ$ , in very good agreement with the analytical prediction of  $90^\circ$ . After all, it is reasonable to expect that for the local flow near the nose, the downstream portion of the body can be approximated as infinitely long,<sup>12</sup> and the good agreement that we observe supports this notion.

More generally, the opening-angle measurement provides a metric to characterize body shape, and we can apply the same procedure to the experimental interfaces to make a comparison. In Fig. 9(b), we plot in black the measurement of  $\Psi$  during the experiment.<sup>32</sup> Initially, both experiment and simulation show a similar decrease in  $\Psi$ , as the wedge front begins to develop. At longer times the two measurements differ, and the experimentally measured angle approaches roughly  $118^\circ$ , a broader opening angle than seen in the simulations.

There are a few plausible explanations for this discrepancy between the simulation and the experiment. First, increasing uncertainty in the experimental measurements caused by turbid water, a smaller body, and focusing issues (which may become more prominent as the initial body taper deteriorates, see Sec. II) may account for the broader angle measurements. On the other hand, the experimental measurements may be accurate and result from a genuine physical effect that is not captured by our model. One possible mechanism is plasticity of the clay, which could allow the nose to be pushed inward by the relatively high pressure at the stagnation point. Preliminary measurements of the clay's yield stress suggest that the hydrodynamic pressure would not cause significant deformation, although absorption of water during the experiments may soften the clay. Another possible mechanism is small-scale flow fluctuations which could cause the position of the stagnation point to wander along the body's nose. In this way, the flow fluctuations could create a smoothing effect on the body. Yet another possibility is that the clay dissolves slowly in water, and that this dissolution occurs preferentially at sites of high curvature.<sup>11</sup> Each of these mechanisms would seem to be consistent with the broader opening angle measurements observed in the experiments. We point out that some of these effects might be captured by the curvature-dependent interface evolution that we included in our simulations, and we discuss this possibility further in Sec. VI. Unsurprisingly, we have noticed that increasing the magnitude of the curvature term in our simulations does produce broader opening angles which are more consistent with the experimental measurements.

### C. Drag on the eroding body

What other unique properties might the attracting geometry possess? An interesting hypothesis is that the flow might reshape the body to reduce drag,<sup>4</sup> as occurs, for example, when a leaf (elastic structure) bends in a stiff breeze.<sup>33,34</sup> Our *separated* flow model permits calculation of drag, allowing us to test this hypothesis. For the high-Re regime considered here, form drag (i.e., pressure drag) dominates over viscous drag, which allows the total drag to be approximated as

$$F_D = \int_{\partial B} p \sin \theta \, ds. \quad (27)$$

Here,  $\sin \theta$  is the  $x$ -component of  $-\hat{n}$ , with  $\theta = \theta(s)$  being the local tangent angle. In Fig. 10(a), we plot the drag on the eroding body of Fig. 6(a), showing that, overall, the drag decreases as the

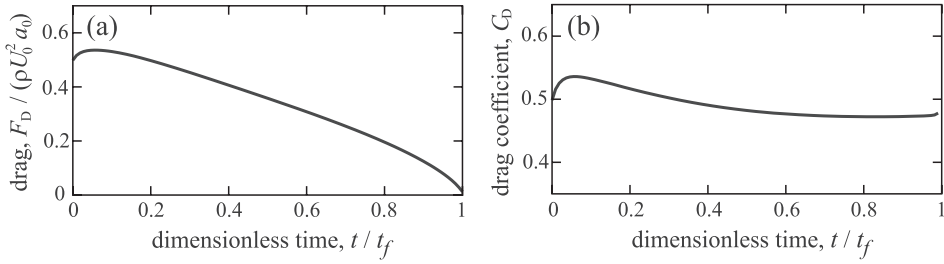


FIG. 10. Drag on an eroding body. (a) Drag versus time for the simulated body of Fig. 6(a), normalized by the fixed value  $\rho U_0^2 a_0$ . After a transient increase, drag decreases with decreasing body size. (b) Drag coefficient for the same body, based on the largest transverse half width,  $a(t)$ . The drag coefficient changes by less than 15% over the course of shape evolution, indicating that erosion is not a streamlining process.

body shrinks. The drag coefficient,  $C_D(t) = F_D(t)/(\rho U_0^2 a(t))$ , scales out body size to show how drag depends on shape alone, and in Fig. 10(b), we plot  $C_D$  against time. For the initial, circular geometry, the FST model is known to underpredict  $C_D$  when compared to experiments (by roughly a factor of two) because it does not capture the negative pressure that occurs in the wake.<sup>23,24,35</sup> However, as long as the average wake pressure does not vary much in time, we expect the model to capture qualitatively how  $C_D$  depends on the evolving body shape. As seen in Fig. 10(b),  $C_D$  changes little over the course of evolution, always lying in the range  $0.45 \leq C_D \leq 0.55$ . Evidently, erosion does not lead to significant drag reduction here. In retrospect, this is not surprising as the shape change is due to shear stress which is a viscous effect, while the drag is due primarily to pressure arising from the inviscid outer flow. We note that for a particular Reynolds number, the viscous drag could easily be included in our calculations by integrating the shear stress along the body and using Eq. (20), which shows a  $Re^{-1/2}$  scaling for the relative contribution of viscous drag. For our experiments in which  $Re \sim 10^4$ , the viscous drag accounts for roughly 1% of the total.

A noticeable feature in Fig. 10(b) is the sharp initial increase of  $C_D$ , corresponding to the time when the shape changes most rapidly. Curiously,  $F_D$  itself increases over this short time-scale as well (Fig. 10(a)), implying that the removal of material can increase the drag experienced by the body. This observation, though surprising, can be reconciled with the fact that removing the forward half of a circular cylinder, i.e., creating a semicircular cylinder with the flat face against the flow, is known to increase drag.<sup>36</sup> We note that experimentally measuring drag during erosion is more straightforward with axisymmetric bodies, since in the cylindrical case, the 3D flow near the ends alters the drag as the body shrinks. Preliminary measurements with axisymmetric bodies indicate a similar transient increase in  $F_D$  as that seen in our 2D simulations, and this will be reported separately.

#### D. Other initial geometries

We now explore questions related to how the erosion dynamics may be influenced by initial conditions. For example, do all initializations eventually lead to a similar right-angled front? To address such questions, we consider a class of elliptical geometries in initializing the simulations. In Figs. 11(a) and 11(b), we show the evolution of a broad ellipse and a narrow ellipse relative to the oncoming flow, where each has an initial aspect ratio of 3:2 (major axis to minor axis). For the broad ellipse, the receding front develops slowly (Fig. 11(a)), while the narrow ellipse's front reaches terminal form quickly, after which the front simply translates backwards (Fig. 11(b)). For the narrow ellipse, the slight growing of the body near the back is an artifact of our curvature-dependent regularization. Both cases yield a similar terminal form, as is demonstrated in Fig. 11(c) by rescaling the shapes that are produced at  $t/t_f = 0.9$  by the two elliptical initialization, as well as that produced by the circular initialization. By this time, all three have produced nearly identical shapes, indicating that memory of the initial condition has been lost.

We show in Fig. 12 the opening angle measurements for each initial condition. The opening angle reaches an asymptote more quickly for a narrow ellipse than it does for a broad ellipse, agreeing

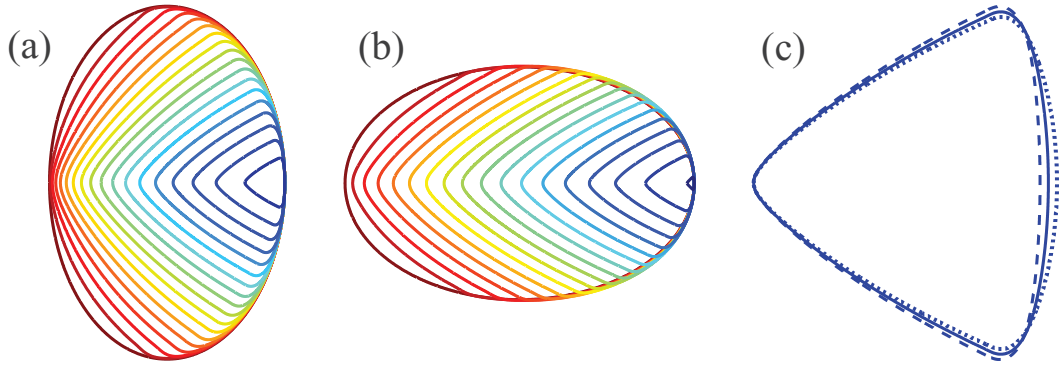


FIG. 11. Simulated erosion of initially elliptical bodies. (a) Evolution of a broad ellipse (major axis perpendicular to the flow) with aspect ratio 3:2. Interfaces are shown at equally spaced time intervals of  $0.06t_f$ , with the same color coding as Fig. 6. (b) Evolution of a narrow ellipse initialization (major axis parallel to the flow, same aspect ratio). (c) Overlaying the interfaces from three different initializations at time  $t/t_f = 0.9$  shows that all tend to a similar shape. Initializations are broad ellipse (dashed), narrow ellipse (dotted), and circle (solid). Running the simulations past  $t/t_f = 0.9$  leads to further collapse of the shapes.

with our observations above. All three initializations result in a final opening angle of nearly  $90^\circ$ , suggesting the uniform-stress morphology to have a large basin of attraction.

### E. Perturbing the attracting geometry

The results above show the wedge-like geometry emerges robustly from different initial conditions. To analyze the attraction in a more local sense, we consider the effect of adding small surface perturbations to the wedge geometry, both in the experiments and simulations. First, to accomplish this in the experiments, we allow erosion to shape the body for roughly an hour, after which we modify its shape by hand. As seen in Fig. 13(a), we add clay to create a protrusion on the top-half of the body, while on the bottom-half we remove clay to create an indentation. We then restart the flow and observe the evolution of the altered body. As shown in Fig. 13(a), the hand-made perturbations decay relatively quickly, on a time-scale of 5–10 min. As hypothesized previously,<sup>12</sup> this experiment confirms the presence of a stabilizing mechanism in the flow-structure interaction: protrusions on the body experience higher shear stress and therefore erode more quickly, while the opposite is true for indentations.

The simulation offers a more controlled setting for observing the fate of such surface perturbations. To initialize the perturbed interface, we run the simulation until the attracting geometry is obtained, and then add a perturbation of the form  $\eta_0(s) = h_0 \cos(2\pi k_0 s/L)$ . Figure 13(b) shows the evolution of such a perturbed interface, with  $h_0 = 0.19$  and  $k_0 = 8$ . The perturbations decay on a short time-scale, much like was seen in the experiments. To understand how erosion removes the

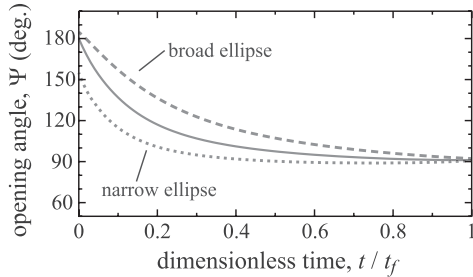


FIG. 12. Measurements of the opening angle,  $\Psi$ , against time for initial geometries of a narrow-side ellipse (dotted curve), broad-side ellipse (dashed curve), and circle (solid curve) in the simulation. The opening angle tends to roughly  $90^\circ$  in each case.

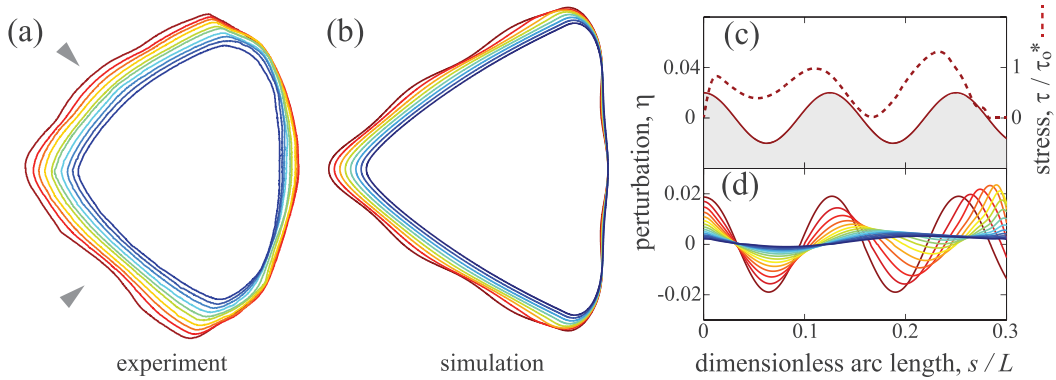


FIG. 13. The evolution of surface perturbations in experiments and simulations. (a) In experiments, a manually added protrusion (top arrow) and indentation (bottom arrow) are seen to even out as the body erodes. Interfaces are shown at intervals of 2 min, over a total of 20 min. (b) Adding a small-amplitude sinusoidal perturbation to the attracting geometry in the simulation shows similar perturbation decay. (c) For the simulated body, plotting the shear stress against arc length on top of the initial perturbation shows the stress to be highest on the front face of each crest. (d) Plotting the evolving perturbation relative to the background interface reveals that the perturbations propagate downstream in addition to the decay.

perturbations, we plot in Fig. 13(c) the shear stress resulting from the initial perturbation  $\eta_0$ . The shear stress is actually highest on the front face of each perturbation, rather than at the peak as might have been expected from the rapid decay of the perturbations. This suggests that as the perturbations wear preferentially on their front, they would also propagate downstream. To test this idea, we plot in Fig. 13(d) the evolution of the perturbation itself,  $\eta(s, t)$ , relative to the receding background interface. As seen in the figure, perturbations do indeed propagate downstream, somewhat reminiscent of granular-bed patterns (such as sand dunes and ripples), which have also been observed to propagate downstream.<sup>37–39</sup> For the granular case, downstream propagation has been predicted by turbulent flow models<sup>39–41</sup> as well as models that rely on triple-deck boundary-layer theory.<sup>16,42</sup> Our results show this behavior to arise in a somewhat different context – gravity is absent, there is no redeposition, and the material is cohesive – suggesting that the effect is robust. Interestingly, in the current configuration, Fig. 13(d) shows that perturbations further back on the body propagate faster, which indicates that the dispersion relation is spatially dependent.

## VI. DISCUSSION

Here we have created a simplified setting for examining certain essential features of the erosion process – most prominently the interaction between shape and flow. Our experiments and simulations of bodies eroding in high-speed flows reveal the emergence of a quasi-triangular geometry that shrinks self-similarly in time. Rather than smoothing shape, erosion tends to reshape the body to more evenly distribute the shear stress along its surface. In long time, the body’s entire front surface tends to a form that produces uniform shear stress, and this shape bears close resemblance to the right-angled wedge predicted by our analytical solutions. Our experiments and simulations show this form to be a stable attractor that emerges robustly from different initial conditions.

Interestingly, the development of this unique shape should not be limited to the linear constitutive law of Eq. (1). Bodies that are either composed of other materials or exposed to other flow regimes may erode according to a nonlinear law,  $V_n = -f(|\tau|)$ , for example, a power law.<sup>15,16</sup> In this case, a shape that produces uniform shear stress would also produce uniform erosion rate. Thus, as long as  $f$  is an increasing function of  $|\tau|$ , we would expect a cylindrical body eroding in a fast, unidirectional flow to develop the same right-angled front, although differences would be expected in the transient evolution and in the power-law that describes self-similar shrinking.

More broadly, natural environments exhibit great complexity, both in the types of flows and the types of materials that are encountered. For example, a single landform may consist of a distribution of soils and sediments having varying erodibility. This variability would distinguish between the

principle of uniform shear stress and that of uniform erosion rate. One could imagine that soft material would erode rapidly, exposing harder material to high shear stress, and that hard material would shield soft material from the flow, causing these regions to experience relatively low shear stress. For a quasi-steady morphology to emerge from this process, variations in shear stress would have to counterbalance variations in erodibility to produce a *uniform erosion rate*. In fact, the principle of uniform erosion rate has been proposed in geological models of dynamic equilibrium.<sup>43</sup> Recently, the principle has been successfully used to understand the morphology of streams that are fed by ground-water flow,<sup>44</sup> and has been supported by direct measurements of erosion rates in certain drainage basins.<sup>45,46</sup> The present study demonstrates the robust emergence of uniform erosion rate in a highly controlled setting, with a theoretical interpretation in terms of laminar boundary layer theory. Furthermore, our findings negate what could be viewed as an alternative hypothesis – that erosion tends to reshape structures so as to reduce drag.<sup>4</sup>

While our Prandtl-based simulations proved to be robust, there are ways in which the model could be improved. Most notably, the model does not capture erosion in the wake of the body. Direct numerical simulations of the Navier-Stokes equations could be used to examine the irregular and time-dependent flow in the wake, and what effect it has on erosion. These effects would play an important role in complicated settings such as the erosion of multiple bodies. Second, our model neglects the interaction between the outer and inner flow that occurs at separation. While we rely on the fact that the size of the interaction region vanishes for  $Re \rightarrow \infty$ , other models, such as interacting boundary layer<sup>16</sup> or triple-deck theory,<sup>19,42</sup> could be used to provide a more complete description for a given, finite  $Re$ .

Finally, in simulating the erosion of a solid body, we introduced a curvature dependence into the interface evolution. Although this was done strictly for regularity of the numerical methods, we found that it reproduced certain features observed in our experiments, such as the roundedness of the nose and separation corners seen on the terminal body (Figs. 6(b) and 6(c)). In fact, we have noticed that increasing the smoothing parameter,  $\varepsilon$ , produces more rounded interfaces that bear even closer resemblance to the experimental shapes and that exhibit broader angle measurements. Furthermore, Fig. 8(a) shows that at the nose of the terminal geometry, the shear stress is relatively low but the interface velocity is maximal. The difference is due entirely to the curvature term, and the resulting interface-velocity distribution agrees qualitatively with our experimental measurements (see Fig. 8(b)). Given these observations, it seems reasonable that the curvature term may account for some real physical mechanism that is present in the experiments but not explicitly included in our model. Small-scale flow fluctuations or slow dissolution of clay in water are two such mechanisms that could cause high-curvature regions to experience increased effective erodibility. Many processes of phase change, such as melting, dissolution, solidification, and evaporation, depend on interfacial curvature,<sup>11</sup> and it seems reasonable that erosion might also belong to this class. More investigation would be required to determine if this is in fact the case, and if so, what is the exact origin of the curvature dependence.

## ACKNOWLEDGMENTS

We would like to thank Alexander Petroff, Tycho Sleator, Eric Keaveny, Adam Stinchcombe, Jacob Bedrossian, and Lisa Fauci for fruitful discussions. This work was partially supported by the NFS (DMS-1103876 and MRI-0821520) and the DOE (DE-FG02-88ER25053).

## APPENDIX: NUMERICAL METHODS

We now provide further details of the numerical methods used in the simulations. The key components are the FST method for the outer flow, the VKP method for the boundary layer flow, and the  $\theta$ - $L$  method for boundary evolution. To demonstrate their dependence on physical parameters, we describe the methods in terms of dimensional quantities. In implementation, however, we use dimensionless quantities, and this can be accomplished by setting  $U_0$ ,  $a_0$ ,  $v$ , and  $\rho$  equal to unity in the description that follows.

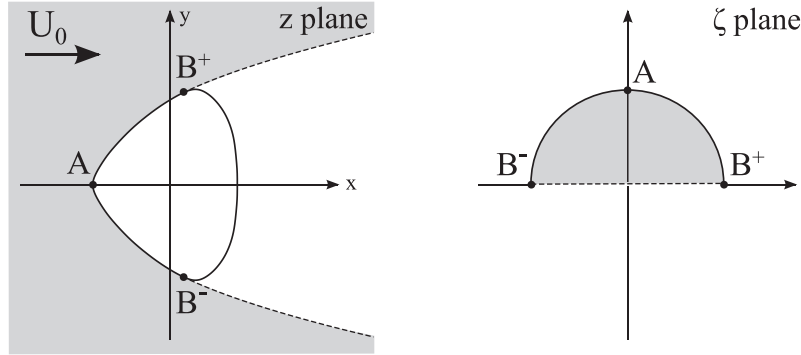


FIG. 14. The conformal mapping method of Levi-Civita. The outer flow domain, indicated by the gray region in the  $z$ -plane, is conformally mapped to the upper-half-unit disk of the  $\zeta$ -plane. The portion of the boundary not in the wake is mapped to the perimeter of the disk,  $\zeta = e^{i\xi}$ , with the stagnation point,  $A$ , mapped to  $\zeta = i$ . The free streamlines are mapped to the diameter of the disk,  $-1 \leq \zeta \leq 1$ , with the separation points,  $B^\pm$ , mapped to  $\zeta = \pm 1$ .

### 1. Free-streamline theory for the outer flow

Our FST method determines the positions of the free streamlines, along with the velocity potential,  $\phi$ , through the numerical solution of Eqs. (6)–(8), and (18). For the moment we treat the separation point,  $s_0$ , as a given, while ultimately we will use the BV condition to determine this point. Following previous studies,<sup>20,21</sup> we use the Levi-Civita conformal mapping method. We introduce a complex potential  $w(z) = \phi + i\psi$ , where  $z = x + iy$ , i.e., the physical coordinates in the flow domain. Here,  $\psi$  is the harmonic conjugate of  $\phi$ , implying that it is the stream-function of the flow.<sup>47</sup> We introduce the log-hodograph variable,  $\Omega = i \log dw/dz$ , with real and imaginary parts  $\Omega = \Omega_R + i\Omega_I$ . The velocity field is given by

$$\mathbf{u}_o = U_0 \overline{dw/dz} = U_0 \exp(\Omega_I + i\Omega_R), \quad (\text{A1})$$

where the bar denotes complex conjugate. As expressed in this formula,  $\Omega_R$  determines the direction of the flow and  $\Omega_I$  determines its magnitude. We will conformally map the outer flow domain, described by  $z$ , to the interior of the upper-half disk, described by  $\zeta$ , as shown in Fig. 14. We express this map as a composition of two maps, with the intermediate variable  $w$  (the complex potential). The map between  $w$  and  $\zeta$  is explicit,

$$w = (C_1/8)(\zeta + 1/\zeta)^2. \quad (\text{A2})$$

Here  $C_1$  is a positive constant that will be determined later. Equations (A1) and (A2) give

$$dz = (C_1/4) e^{i\Omega} (\zeta - 1/\zeta^3) d\zeta. \quad (\text{A3})$$

On the perimeter of the upper-half disk, let  $\zeta = e^{i\xi}$  where  $0 \leq \xi \leq \pi$ . Let  $\theta_f(\xi) = \Omega_R(\zeta)$  and  $\mu(\xi) = \Omega_I(\zeta)$ , so that  $\theta_f$  corresponds to the flow direction and  $\mu$  the flow magnitude. From Eq. (A3), the arc-length increment along the body  $ds$  is given by

$$ds = (C_1/2) e^{-\mu} |\sin 2\xi| d\xi. \quad (\text{A4})$$

We express  $\Omega$  as a Taylor series,

$$\Omega = \sum_{k=0}^{\infty} a_k \zeta^k. \quad (\text{A5})$$

This implies the following cosine and sine series for  $\theta_f$  and  $\mu$ :

$$\theta_f = \sum_{k=0}^{\infty} a_k \cos k\xi, \quad (\text{A6})$$

$$\mu = \sum_{k=1}^{\infty} a_k \sin k\xi. \quad (\text{A7})$$

The flow changes direction across the front stagnation point, leading to a discontinuity in  $\theta_f$  at  $\xi = \pi/2$ . To remove this singularity, we let  $\Omega = \Omega_s + \tilde{\Omega}$ , where  $\tilde{\Omega}$  is the desingularized form and the singular part is given by

$$\Omega_s = \theta_s + i\mu_s = \pi + i \log \frac{e^{i\xi} - i}{e^{i\xi} + i}, \quad (\text{A8})$$

$$\theta_s = \frac{\pi}{2} \operatorname{sign}(\xi - \pi/2), \quad (\text{A9})$$

$$\mu_s = \log |\tan(\xi/2 - \pi/4)|. \quad (\text{A10})$$

Integrating the desingularized form of Eq. (A4) gives

$$s(\xi) = C_1 \int_{\pi/2}^{\xi} (\sin \xi' + \sin^2 \xi') e^{-\tilde{\mu}(\xi')} d\xi', \quad \text{for } 0 \leq \xi \leq \pi. \quad (\text{A11})$$

Finally, enforcing  $s(\pi) = s_0$  (the separation point) determines the constant  $C_1$ .

Due to boundary condition (7), the outer flow is always tangential to the surface. Thus, for a given up-down symmetric geometry, the dependence of  $\theta_f$  on  $s$  is known, allowing us to solve Eq. (A11) by Picard iteration. We begin with a guess for  $s(\xi)$ , e.g.,  $s(\xi) = s_0(2\xi/\pi - 1)$ , and use Hermite interpolation to determine the corresponding function  $\theta_f(\xi)$  on a uniform  $\xi$ -grid. We then determine the coefficients  $a_k$  in Eq. (A6) and the corresponding function  $\mu(\xi)$  in Eq. (A7) through the use of discrete cosine and sine transforms; in implementation this process is actually applied to the desingularized forms,  $\tilde{\theta}_f$ ,  $\tilde{\mu}$ , and  $\tilde{a}_k$ . Next, we numerically integrate Eq. (A11) with the computed  $\tilde{\mu}$  to obtain an updated  $s(\xi)$ , and iterate until convergence.

To determine the outer flow, we use the mapping  $s \leftrightarrow \xi$  and insert the computed values of  $\Omega_R = \theta_f(\xi)$  and  $\Omega_I = \mu(\xi)$  into Eq. (A1). This gives the outer, tangential velocity as

$$U = U_0 e^\mu = U_0 \tan(\xi/2 - \pi/4) e^{\tilde{\mu}}. \quad (\text{A12})$$

The quantity  $dU/ds$  also appears in the Prandtl Eq. (10). To compute  $dU/ds$ , we differentiate Eq. (A12) with respect to  $\xi$  and use the chain rule with  $d\xi/ds$  computed from Eq. (A11), to arrive at

$$\frac{dU}{ds} = \frac{U_0 e^{2\tilde{\mu}}}{C_1 (\sin \xi + \sin^2 \xi)} \left( \frac{1}{1 + \sin \xi} + \frac{d\tilde{\mu}}{d\xi} \tan(\xi/2 - \pi/4) \right). \quad (\text{A13})$$

Since we are only interested in computing the shear stress on the boundary, these two quantities,  $U$  and  $dU/ds$ , are all that is needed from the FST method.

We now address how to choose  $s_0$  so as to satisfy the BV condition. For a generic separated flow, the pressure gradient exhibits a singularity of type  $(s - s_0)^{-1/2}$  at separation. Asymptotic analysis shows that satisfying the BV condition, i.e., requiring the free-streamline curvature to match the body curvature at separation, is equivalent to removing this singularity in the pressure gradient.<sup>19</sup> Further, Bernoulli's Eq. (17) shows this to be equivalent to removing the singularity in  $dU/ds$  in Eq. (A13) at the point  $\xi = \pi$ , which is how our method enforces in the BV condition.

When coupling the outer flow to the boundary layer flow, an adverse pressure gradient,  $dp/ds > 0$ , is needed near  $s_0$  to force boundary layer separation. This adverse pressure gradient can be achieved by moving  $s_0$  slightly downstream of what the BV condition requires. Thus, instead of enforcing the BV condition exactly,  $dU/ds = 0$  at  $\xi = \pi$ , we require (the dimensionless)  $dU/ds$  to take a fixed, negative value (we use  $-12$ ) at the last grid point before  $\xi = \pi$ . Through Bernoulli's equation, this ensures  $dp/ds > 0$  there. Our choice of the value  $-12$  is not special; any negative value will do since  $dU/ds$  is generically singular at  $\xi = \pi$ , and thus increasing the grid-resolution moves  $s_0$  arbitrarily close to the BV requirement, while still allowing separation of the boundary layer.

In implementation, we iterate our FST method with a nonlinear root find to enforce this desired condition on  $dU/ds$ .

In reality, flow separation is associated with a so-called interaction region, where the boundary layer flow feeds back to the outer flow. Asymptotic analysis relying on triple-deck boundary layer theory<sup>48,49</sup> has demonstrated that as  $\text{Re} \rightarrow \infty$ , the size of the interaction region vanishes and the BV condition accurately predicts the point of flow separation.<sup>19</sup> As such, our use of the BV condition obviates the need for a more sophisticated interaction model, and the simplicity of the condition allows for seamless integration of FST and boundary layer theory.

## 2. The von Kármán-Pohlhausen method for the inner flow

Given the outer flow quantities,  $U$  and  $U' = dU/ds$ , we use the VKP method<sup>18,27,28</sup> to approximate the solution to the Prandtl equations and boundary conditions given in Eqs. (10)–(15). We introduce the displacement and momentum thickness,  $\delta_d$  and  $\delta_m$ , defined by

$$\delta_d(s) = \int_0^\infty \left(1 - \frac{u}{U}\right) dn, \quad (\text{A14})$$

$$\delta_m(s) = \int_0^\infty \frac{u}{U} \left(1 - \frac{u}{U}\right) dn. \quad (\text{A15})$$

Balancing the local momentum flux via vertically integration of the Prandtl PDEs results in the relation<sup>18</sup>

$$\frac{\tau}{\rho U^2} = \delta'_m + (2\delta_m + \delta_d) \frac{U'}{U}. \quad (\text{A16})$$

Within the Prandtl framework, this is an exact relationship, and it forms the basis of the VKP approximation method which we now describe.

Appealing to a similarity Ansatz, let  $u(s, n) = U(s)F(\eta)$ , where  $\eta = n/\delta_e(s)$  and  $\delta_e(s)$  is an effective boundary layer thickness that will be computed to satisfy Eq. (A16). In the VKP method, we approximate  $F(\eta)$  by a fourth-order polynomial. Satisfying boundary conditions (13)–(15), along with smoothness of the velocity profile across the boundary layer, gives the form of the polynomial,

$$F(\eta) = \eta(2 - 2\eta^2 + \eta^3) + \frac{\Lambda}{6}\eta(1 - \eta)^3. \quad (\text{A17})$$

Here,  $\Lambda$  is a dimensionless quantity chosen to satisfy Eq. (15),

$$\Lambda(s) = \frac{\delta_e^2 U'}{\nu}. \quad (\text{A18})$$

For convenience, we introduce the following dimensionless quantities:

$$H(s) = \frac{\delta_d}{\delta_m}, \quad (\text{A19})$$

$$S(s) = \frac{\delta_m \tau}{\nu \rho U}, \quad (\text{A20})$$

$$\lambda(s) = \frac{\delta_m^2 U'}{\nu} = \Lambda \frac{\delta_m^2}{\delta_e^2}. \quad (\text{A21})$$

These are known, respectively, as the shape factor  $H$ , the shear function  $S$ , and the Holstein-Bohlen dimensionless parameter  $\lambda$ . Multiplying Eq. (A16) by  $\delta_m$  and rearranging gives the ODE,

$$\frac{d}{ds} \left( \frac{\lambda}{U'} \right) = \frac{2}{U} (S - \lambda(H + 2)). \quad (\text{A22})$$

Inserting Eq. (A17) into Eqs. (A14) and (A15) gives the following expressions for  $H$ ,  $S$ , and  $\lambda$  in terms of  $\Lambda$  alone,

$$H = \frac{315}{10} \frac{3 - \Lambda/12}{q(\Lambda)}, \quad (\text{A23})$$

$$S = \frac{2}{315} \left( 1 + \frac{\Lambda}{12} \right) q(\Lambda), \quad (\text{A24})$$

$$\lambda = \frac{\Lambda}{315^2} q(\Lambda)^2, \quad (\text{A25})$$

$$q = 37 - 4 \left( \frac{\Lambda}{12} \right) - 5 \left( \frac{\Lambda}{12} \right)^2. \quad (\text{A26})$$

Using these relations, we integrate Eq. (A22) with a fourth-order Runge-Kutta method. Since  $U(0) = 0$ , the ODE is singular at  $s = 0$ , i.e., at the stagnation point, and choosing  $\lambda(0)$  to remove this singularity provides the needed initial condition for the ODE. With  $\lambda(s)$  known through the solution of Eq. (A22), we invert Eq. (A25) to determine  $\Lambda(s)$ , and then compute the shear stress for the profile in Eq. (A17),

$$\tau = 2\sqrt{\nu\rho} U \sqrt{\frac{U'}{\Lambda}} \left( 1 + \frac{\Lambda}{12} \right). \quad (\text{A27})$$

To obtain the dimensionless shear stress,  $\tau/\tau_0^*$ , we simply set  $\nu$ ,  $\rho$ ,  $U_0$ , and  $a_0$  to unity in the above. In the following, we switch to dimensionless variables without changing notation. The outer flow quantities are scaled on  $U_0$  and  $a_0$ , and  $\delta_e$  is scaled on  $\delta_0^*$ .

Separation of the boundary layer occurs when the shear stress vanishes. Ostensibly, Eq. (A27) indicates this may happen if either  $U = 0$ ,  $U' = 0$ , or  $\Lambda = -12$ . However, Eq. (A18) shows that  $U' \rightarrow 0$  implies  $\Lambda \rightarrow 0$  also, and in fact the shear stress does not vanish. Further, we typically only see  $U = 0$  at the stagnation point. Therefore, boundary layer separation generically requires  $\Lambda = -12$ . Under typical conditions, we observe  $\delta_e > 1$ , from which Eq. (A18) implies that if  $U' = -12$  then  $\Lambda < -12$ , i.e., the boundary layer has separated. This motivates our choice of requiring  $U' = -12$  at the last grid point before  $s_0$  in enforcing the BV condition.

A few comments on implementation are in order. First, as already noted, Eq. (A27) has a removable singularity wherever  $U' = 0$ . Therefore, in evaluating the shear stress near such a point, we replace  $U'/\Lambda$  with  $37^2 U'/(315^2 \lambda)$ , which follows from taking  $\Lambda \rightarrow 0$  in Eq. (A25);  $\lambda/U'$  is always well-behaved since it is the quantity that is computed directly in ODE (A22). Next, to compute  $V_n$  we need the quantity  $|\tau|$ , which generically has a discontinuous first derivative where  $\tau$  changes sign. Over the course of evolution, these discontinuities would lead to a geometry that is not smooth at the stagnation point and at the separation points. We therefore apply a narrow Gaussian filter in  $s$  to the distribution  $|\tau|$  that is computed at each time step (we use a filter width of  $\sigma = 0.05$  as defined in Eq. (A40) of Subsection A 3 of the Appendix). The Gaussian filter also moderates oscillations in  $\tau$  that we sometimes observe near separation (where boundary-layer theory loses validity). Finally, the quartic approximation to the velocity profile becomes non-monotonic for  $\Lambda > 12$ , which limits the physical validity of the KPV method. As a symptom of this breakdown, the relationship between  $\lambda$  and  $\Lambda$  in Eq. (A25) becomes non-invertible preventing further integration of ODE (A22). We do not observe this to happen for the initial circular geometry, nor for the final attracting geometry, however during the course of evolution, we occasionally observe  $\Lambda > 12$  over small intervals. To allow integration of the ODE to continue in such cases, we set  $\Lambda = \min(\Lambda, 12)$  in evaluating  $S$  and  $H$  in Eq. (A22). The Gaussian filter controls any non-smoothness in the stress distribution that may result from this truncation.

### 3. Numerical evolution of the boundary: the $\theta$ -L formulation

With the shear stress determined by the inner flow model, the solid boundary evolves according to Eq. (1). In order to prevent a loss of boundary regularity that would result from discontinuities in

$\partial_s |\tau|$ , we will introduce a smoothing term into Eq. (1) that involves the local body curvature  $\kappa$ . As we show below, this leads to a diffusive term appearing in the equation for shape evolution. Such a technique, sometimes called the *method of vanishing viscosity* (not to be confused with the fluid viscosity), is often used to regularize problems involving front propagation.<sup>29,30</sup> For the following, we consider only dimensionless quantities, with interface velocity scaled on  $V_n^*$ , shear stress scaled on  $\tau_0^*$ , and total interface length scaled on  $a_0$ , without changing notation. We modify Eq. (1) to read

$$V_n = -|\tau| - \varepsilon\sqrt{L} \left( \kappa - \frac{2\pi}{L} \right). \quad (\text{A28})$$

The material constant  $C$  does not appear in this equation because of our non-dimensionalization. Here,  $\varepsilon$  is the pre-factor for the smoothing term, and the solution to Eq. (A28) is a *viscosity solution* to Eq. (1) in the limit  $\varepsilon \rightarrow 0$ . Informed by Eq. (22), we have also introduced the pre-factor  $\sqrt{L}$ , so that the smoothing term scales like  $|\tau|$  as the body vanishes. Finally, in the parenthesis, we have subtracted the average curvature,  $2\pi/L$ , so that the smoothing term preserves body area, i.e., the only material loss is due to the action of the shear stress.

Rather than tracking the physical coordinates of the boundary, our method evolves the local tangent angle,  $\theta$ , defined by  $(\partial_s x, \partial_s y) = (\cos \theta, \sin \theta)$ , along with the total arc length  $L$ . This approach, known as the  $\theta$ - $L$  method, allows us to use unconditionally stable methods for time evolution, thus mitigating the stiffness introduced by the higher order curvature term.<sup>50</sup> In the  $\theta$ - $L$  method, we let  $\alpha = s/L$  be a normalized arc length, and allow  $\alpha$  to parameterize the boundary via  $X = (x(\alpha), y(\alpha))$ , where  $0 \leq \alpha \leq 1$ ; this is the equal-arc-length parameterization. While the normal velocity,  $V_n$ , is specified by the physics, we are free to introduce an arbitrary tangential velocity  $V_s$ , so that the boundary evolves as

$$\frac{\partial X}{\partial t} = V_n \hat{n} + V_s \hat{s}. \quad (\text{A29})$$

As diagrammed in Fig. 3,  $\hat{n}$  is the outward unit normal, and  $\hat{s}$  is the unit tangent vector running in the clockwise direction. Here, we choose the tangential velocity to keep the curve in the equal-arc-length parameterization by setting<sup>50</sup>

$$V_s = \int_0^\alpha \frac{\partial \theta}{\partial \alpha'} V_n d\alpha' - \alpha \left\langle \frac{\partial \theta}{\partial \alpha} V_n \right\rangle. \quad (\text{A30})$$

In the above, bracket denotes average value, i.e.,  $\langle f \rangle = \int_0^1 f(\alpha') d\alpha'$ . With  $V_n$  and  $V_s$  specified,  $L$  and  $\theta$  evolve according to<sup>50</sup>

$$\frac{dL}{dt} = - \left\langle \frac{\partial \theta}{\partial \alpha} V_n \right\rangle, \quad (\text{A31})$$

$$\frac{\partial \theta}{\partial t} = \frac{1}{L} \left( \frac{\partial V_n}{\partial \alpha} + \frac{\partial \theta}{\partial \alpha} V_s \right). \quad (\text{A32})$$

Using the modified erosion law of Eq. (A28), and noting  $\kappa = -\partial_\alpha \theta / L$ , gives the following evolution equation for  $\theta$ :

$$\frac{\partial \theta}{\partial t} = \varepsilon L^{-3/2} \frac{\partial^2 \theta}{\partial \alpha^2} + L^{-1} \left( -\frac{\partial |\tau|}{\partial \alpha} + \frac{\partial \theta}{\partial \alpha} V_s \right). \quad (\text{A33})$$

The diffusive term in this equation results from the curvature term that was introduced in Eq. (A28). Our task is to numerically evolve  $\theta$  and  $L$  through the coupled Eqs. (A31) and (A33). We treat Eq. (A31) explicitly with second-order Adams-Bashforth method,

$$L^{n+1} = L^n + \frac{\Delta t}{2} (3M^n - M^{n-1}), \quad (\text{A34})$$

where  $M = -(\partial_\alpha \theta V_n)$ . Meanwhile, we solve Eq. (A33) spectrally. We introduce the Fourier series for a function  $f$ ,

$$f(\alpha) = \sum_{k=-\infty}^{\infty} \hat{f}(k) e^{2\pi i k \alpha}. \quad (\text{A35})$$

In spectral space, Eq. (A33) becomes

$$\frac{d\hat{\theta}}{dt} + 4\pi^2 k^2 \varepsilon L^{-3/2} \hat{\theta} = \hat{N}. \quad (\text{A36})$$

Here,  $N = L^{-1}(-\partial_\alpha |\tau| + \partial_\alpha \theta V_s)$  represents the nonlinear terms. To solve this equation, we multiply by the integrating factor  $\exp(4\pi^2 k^2 \varepsilon \int_0^t L^{-3/2} dt')$ , apply the Adams-Bashforth method, and use the trapezoid rule to arrive at

$$\hat{\theta}^{n+1} = e_1 \hat{\theta}^n + \frac{\Delta t}{2} (3e_1 \hat{N}^n - e_2 \hat{N}^{n-1}), \quad (\text{A37})$$

$$e_1 = \exp(-2\pi^2 k^2 \varepsilon \Delta t ((L^n)^{-3/2} + (L^{n+1})^{-3/2})), \quad (\text{A38})$$

$$e_2 = \exp(-2\pi^2 k^2 \varepsilon \Delta t ((L^{n-1})^{-3/2} + 2(L^n)^{-3/2} + (L^{n+1})^{-3/2})). \quad (\text{A39})$$

This integrating-factor method is unconditionally stable, and in fact it can be recast in terms of Gaussian filters. The Gaussian filter is given by

$$\mathcal{G}(f(\alpha), \sigma) = \sum_{k=-\infty}^{\infty} e^{-\frac{1}{2}\sigma^2 k^2} \hat{f}(k) e^{2\pi i k \alpha}, \quad (\text{A40})$$

where  $\sigma$  is the filter width. Equations (A37)–(A39) can then be expressed as

$$\theta^{n+1} = \mathcal{G}(\theta^n, \sigma_1) + \frac{\Delta t}{2} (3\mathcal{G}(N^n, \sigma_1) - \mathcal{G}(N^{n-1}, \sigma_2)), \quad (\text{A41})$$

$$\sigma_1 = 2\pi \sqrt{\varepsilon \Delta t} \sqrt{(L^n)^{-3/2} + (L^{n+1})^{-3/2}}, \quad (\text{A42})$$

$$\sigma_2 = 2\pi \sqrt{\varepsilon \Delta t} \sqrt{(L^{n-1})^{-3/2} + 2(L^n)^{-3/2} + (L^{n+1})^{-3/2}}. \quad (\text{A43})$$

Since  $\mathcal{G}$  is a smoothing transform (as long as  $\sigma$  is positive), this expression makes clear the stability of the time-marching scheme.

In implementation, the boundary evolution proceeds as follows. At step  $n$ , we use  $\theta^n$  and  $V_n$  to compute  $M^n$ , and then update  $L^{n+1}$  through Eq. (A34). We then compute  $V_s$  through Eq. (A30), which is needed to compute  $N^n$ . Finally, with  $L^{n+1}$  known, we can compute  $\sigma_1$  and  $\sigma_2$ , and update  $\theta^{n+1}$  through Eq. (A41). To recover the physical coordinates from the variables  $\theta$  and  $L$ , we specify the back-most point of the body to be fixed, which is motivated by our assumption of a stagnant wake. This choice is equivalent to shifting the body by a small amount (of order  $\varepsilon$ ) in order to enforce  $V_n = 0$  at  $\alpha = 0.5$ . In all of the results presented in Sec. V, we have taken  $\varepsilon = 0.02$ , the number of grid points to be either 2048 or 4096, and a time-step of  $\Delta t = 10^{-4}$ .

As a final comment, Eq. (A32) allows for a nice interpretation of the condition required for the body to maintain its shape during evolution. Strictly speaking, uniform interface velocity does not always lead to shape preservation for a body that has variable curvature. For the attracting quasi-triangular body, piecewise uniform interface velocity provides a useful, but approximate, working principle because each side of the triangular body has roughly constant curvature. In general though, body shape is encoded in the function  $\theta(\alpha)$ , and so the condition for shape preservation is that  $\partial_\alpha \theta = 0$  in Eq. (A32). This equation shows that no matter where  $V_n$  comes from, the local curvature of the body  $\kappa = \partial_\alpha \theta / L$  enters the condition for shape preservation. This observation helps to explain the peak in interface velocity at the nose of the body (where the curvature is high) that is observed in both experiments and simulations (see Fig. 8).

- <sup>1</sup>S. Schumm and H. Khan, "Experimental study of channel patterns," *Geol. Soc. Am. Bull.* **83**, 1755–1770 (1972).
- <sup>2</sup>S. Ikeda, G. Parker, and K. Sawai, "Bend theory of river meanders. Part 1. Linear development" *J. Fluid Mech.* **112**, 363–377 (1981).
- <sup>3</sup>A. Ward, "Yardangs on Mars: Evidence of recent wind erosion," *J. Geophys. Res., [Solid Earth]* **84**, 8147–8166, doi:10.1029/JB084iB14p08147 (1979).
- <sup>4</sup>A. Ward and R. Greeley, "Evolution of the yardangs at Rogers Lake, California," *Geol. Soc. Am. Bull.* **95**, 829–837 (1984).
- <sup>5</sup>A. Scheidegger, "A physical theory of the formation of hoodoos," *Pure Appl. Geophys.* **41**, 101–106 (1958).
- <sup>6</sup>S. Wang, "Coastal hoodoos," *Encyclopedia of Coastal Science* (Springer, Netherlands, 2005), pp. 260–262.
- <sup>7</sup>P. K. Shah, "Pathophysiology of coronary thrombosis: Role of plaque rupture and plaque erosion," *Prog. Cardiovasc. Dis.* **44**, 357–368 (2002).
- <sup>8</sup>H. C. Groen, F. J. Gijsen, A. van der Lugt, M. S. Ferguson, T. S. Hatsukami, A. F. van der Steen, C. Yuan, and J. J. Wentzel, "Plaque rupture in the carotid artery is localized at the high shear stress region: A case report," *Stroke* **38**, 2379–2381 (2007).
- <sup>9</sup>C. Picioreanu, M. C. van Loosdrecht, and J. J. Heijnen, "Two-dimensional model of biofilm detachment caused by internal stress from liquid flow," *Biotechnol. Bioeng.* **72**, 205–218 (2001).
- <sup>10</sup>G. Nanz and L. E. Camilletti, "Modeling of chemical-mechanical polishing: A review," *IEEE Trans. Semiconduct. Manuf.* **8**, 382–389 (1995).
- <sup>11</sup>S. Gupta, *The Classical Stefan Problem: Basic Concepts, Modelling and Analysis* (Elsevier, Amsterdam, 2003).
- <sup>12</sup>L. Ristroph, M. Moore, S. Childress, M. Shelley, and J. Zhang, "Sculpting of an erodible body by flowing water," *Proc. Natl. Acad. Sci. U.S.A.* **109**, 19606–19609 (2012).
- <sup>13</sup>H. Helmholtz, "Über diskontinuierliche Flüssigkeitsbewegungen" *Philos. Mag.* **36**, 337–346 (1868).
- <sup>14</sup>G. Kirchhoff, "Zur Theorie freier Flüssigkeitsstrahlen" *J. Reine Angew. Math.* **70**, 289–298 (1869).
- <sup>15</sup>G. Parker and N. Izumi, "Purely erosional cyclic and solitary steps created by flow over a cohesive bed," *J. Fluid Mech.* **419**, 203–238 (2000).
- <sup>16</sup>P.-Y. Lagrée, "Erosion and sedimentation of a bump in fluvial flow," *C. R. Acad. Sci., Ser. IIB Mech.* **328**, 869–874 (2000).
- <sup>17</sup>H. Schlichting, *Boundary Layer Theory* (McGraw-Hill, New York, 1960).
- <sup>18</sup>C. Pozrikidis, *Introduction to Theoretical and Computational Fluid Dynamics* (Oxford University Press, New York, 1997).
- <sup>19</sup>V. V. Sychëv, A. I. Ruban, V. V. Sychev, and G. L. Korolev, *Asymptotic Theory of Separated Flows* (Cambridge University Press, Cambridge, 1998).
- <sup>20</sup>J. Hureau, E. Brunon, and P. Legallais, "Ideal free streamline flow over a curved obstacle," *J. Comput. Appl. Math.* **72**, 193–214 (1996).
- <sup>21</sup>S. Alben, M. Shelley, and J. Zhang, "How flexibility induces streamlining in a two-dimensional flow," *Phys. Fluids* **16**, 1694–1713 (2004).
- <sup>22</sup>G. Batchelor, "A proposal concerning laminar wakes behind bluff bodies at large Reynolds number," *J. Fluid Mech.* **1**, 388 (1956).
- <sup>23</sup>G. Parkinson and T. Jandali, "A wake source model for bluff body potential flow," *J. Fluid Mech.* **40**, 577–594 (1970).
- <sup>24</sup>T. Wu, "Cavity and wake flows," *Annu. Rev. Fluid Mech.* **4**, 243–284 (1972).
- <sup>25</sup>M. Brilouin, "Les surfaces de glissement d'Helmholtz et la résistance des fluides," *Ann. Chim. Phys.* **23**, 145–230 (1911).
- <sup>26</sup>H. Villat, "Sur la validité des solutions de certains problèmes d'hydrodynamique," *J. Math. Pures Appl.* **10**, 231–290 (1914).
- <sup>27</sup>T. V. Kármán, "Über laminaire und turbulente Reibung," *Z. Angew. Math. Mech.* **1**, 233–252 (1921).
- <sup>28</sup>K. Pohlhausen, "Zur näherungsweisen Integration der Differentialgleichung der laminaren Grenzschicht," *Z. Angew. Math. Mech.* **1**, 252–268 (1921).
- <sup>29</sup>M. G. Crandall and P.-L. Lions, "Viscosity solutions of Hamilton-Jacobi equations," *Trans. Am. Math. Soc.* **277**, 1–42 (1983).
- <sup>30</sup>J. A. Sethian, *Level Set Methods and Fast Marching Methods: Evolving Interfaces in Computational Geometry, Fluid Mechanics, Computer Vision, and Materials Science* (Cambridge University Press, Cambridge, 1999), Vol. 3.
- <sup>31</sup>V. M. Falkner and S. W. Skan, "Solutions of the boundary layer equations," *Philos. Mag.* **12**, 865–896 (1931).
- <sup>32</sup>Here we normalize time by  $t^* = 2a_0/V_n^*$ , where  $V_n^* = 1 \text{ cm/hr}$  for the experiments, as opposed to normalizing by  $t_f$ . The quantity  $t^*$  estimates the vanishing time in the case of no erosion on the backside of the body, allowing a more faithful comparison between the experimental and simulated front evolution.
- <sup>33</sup>S. Vogel, "Drag and reconfiguration of broad leaves in high winds," *J. Exp. Bot.* **40**, 941–948 (1989).
- <sup>34</sup>S. Alben, M. Shelley, and J. Zhang, "Drag reduction through self-similar bending of a flexible body," *Nature (London)* **420**, 479–481 (2002).
- <sup>35</sup>E. Achenbach, "Distribution of local pressure and skin friction around a circular cylinder in cross-flow up to  $\text{Re} = 5 \times 10^6$ ," *J. Fluid Mech.* **34**, 625–639 (1968).
- <sup>36</sup>W. P. Graebel, *Engineering Fluid Mechanics* (Taylor and Francis, New York, 2001).
- <sup>37</sup>F. Engelund and J. Fredsoe, "Sediment ripples and dunes," *Annu. Rev. Fluid Mech.* **14**, 13–37 (1982).
- <sup>38</sup>A. Fowler, "Dunes and drumlins," *Geomorphological Fluid Mechanics* (Springer, Berlin, 2001), pp. 430–454.
- <sup>39</sup>F. Charru, B. Andreotti, and P. Claudin, "Sand ripples and dunes," *Annu. Rev. Fluid Mech.* **45**, 469–493 (2013).
- <sup>40</sup>K. Kroy, G. Sauermann, and H. J. Herrmann, "Minimal model for sand dunes," *Phys. Rev. Lett.* **88**, 054301 (2002).
- <sup>41</sup>K. Kroy, G. Sauermann, and H. J. Herrmann, "Minimal model for aeolian sand dunes," *Phys. Rev. E* **66**, 031302 (2002).
- <sup>42</sup>P.-Y. Lagrée, "A triple deck model of ripple formation and evolution," *Phys. Fluids* **15**, 2355 (2003).
- <sup>43</sup>J. T. Hack, "Dynamic equilibrium and landscape evolution," *Theories of Landform Development* (State University of New York, 1975), pp. 87–102.
- <sup>44</sup>O. Devauchelle, A. Petroff, A. Lobkovsky, and D. Rothman, "Longitudinal profile of channels cut by springs," *J. Fluid Mech.* **667**, 38–47 (2011).

- <sup>45</sup>D. Burbank, A. Blythe, J. Putkonen, B. Pratt-Sitaula, E. Gabet, M. Oskin, A. Barros, and T. Ojha, “Decoupling of erosion and precipitation in the Himalayas,” *Nature (London)* **426**, 652–655 (2003).
- <sup>46</sup>A. Matmon, P. Bierman, J. Larsen, S. Southworth, M. Pavich, and M. Caffee, “Temporally and spatially uniform rates of erosion in the southern Appalachian Great Smoky Mountains,” *Geology* **31**, 155–158 (2003).
- <sup>47</sup>R. Camassa, R. M. McLaughlin, M. N. J. Moore, and A. Vaidya, “Brachistochrones in potential flow and the connection to Darwin’s theorem,” *Phys. Lett. A* **372**, 6742–6749 (2008).
- <sup>48</sup>V. Sychev, “Laminar separation,” *Fluid Dyn.* **7**, 407–417 (1972).
- <sup>49</sup>R. Meyer, “A view of the triple deck,” *SIAM J. Appl. Math.* **43**, 639–663 (1983).
- <sup>50</sup>T. Hou, J. Lowengrub, and M. Shelley, “Removing the stiffness from interfacial flows with surface tension,” *J. Comput. Phys.* **114**, 312–338 (1994).